Silicon-on-Insulator Nanowire Resonators for Compact and Ultra-High Speed All-Optical Wavelength Converters

Christos Stamatiadis, Konstantinos Vyrsokinos, Leontios Stampoulidis, Ioannis Lazarou, Alexandros Maziotis, Jens Bolten, Matthias Karl, Thorsten Wahlbrink, Peter De Heyn, Zhen Sheng, Dries Van Thourhout, and Hercules Avramopoulos

Abstract—We present the development of application-specific silicon-on-insulator SOI nanowire ring and racetrack resonators designed to assist semiconductor optical amplifier (SOA)-based all-optical wavelength conversion. We demonstrate the fabrication of fix resonance racetrack resonators exhibiting coupling gaps as low as 160 nm and tunable ring resonators with coupling gaps <90 nm. The resonators are cascaded after commercial 40 Gb/s SOAs to realize chirp filtering of the optical data signals through high-resolution spectral sampling. We experimentally demonstrate inverted and non-inverted SOI resonator-assisted all-optical wavelength conversion at 40 Gb/s and 160 Gb/s with power penalties <3 dB.

Index Terms—Microring resonators, optical signal processing, photonic integration, reconfigurable add-drop multiplexers, semiconductor optical amplifiers (SOAs), wavelength converters.

I. INTRODUCTION

SILICON-on-insulator (SOI) has been considered the material of choice for nanophotonic integration [1]. The promising optical properties of SOI together with the complementary metal–oxide–semiconductor (CMOS)-compatible fabrication of optical waveguides have stimulated world-wide research efforts for the implementation of ultra-compact and high-density photonic integrated circuits [2]–[6]. In this context, the SOI nanowire waveguide platform has been utilized for the integration of components applicable to wavelength division multiplexing (WDM) and chip-scale photonic interconnect networks [7]. In these applications, high-order microring resonators are used to realize add/drop wavelength selective functionalities where high-resolution filtering, bandpass flatness, and superior crosstalk are required. Beyond channel add-drop filtering, these passive microresonator structures have been recently demonstrated to assist switching [8], buffering [9], modulation [10], and all-optical wavelength conversion (AOWC) [11] for next generation photonic routing systems.

In the case of semiconductor optical amplifier (SOA)-based microresonator-assisted wavelength converters, medium index contrast microring resonators with bending sections ∼50 μm have proven the potential for effective chirp-filtering and WDM-enabled AOWC operation at 40 Gb/s [12]. In order to enable even faster bit rates, higher order coupled resonators are required. These resonators must exhibit microscale radius, ultra-sharp spectral profiles, and round-trip times comparable to the applied ultra-short pulsewidths, and the SOI nanowire platform is ideal for meeting these requirements. In [13], we have reported the first experimental evidence on SOA-based 160 Gb/s wavelength conversion (WC) assisted by a third-order SOI nanowire racetrack resonator with a box-shaped spectral profile. The choice of a racetrack was due to the high interaction length of the waveguides (bus–racetrack and racetrack–racetrack) that allows high coupling coefficients with coupling gaps as high as 160 nm (bus–racetrack) and 280 nm (racetrack–racetrack), respectively.

In this paper, we present the detailed design, fabrication, and experimental demonstration of second- and third-order add/drop SOI microresonator structures for AOWC. All the components were fabricated using high-resolution e-beam lithography for patterning 220×450 nm waveguides on 30 mm × 30 mm SOI chips. Two different component generations are presented; fixed resonance racetrack resonators with 50% efficient fiber coupling through input-output SU8 tapers and tunable ring resonators with 30% efficient fiber coupling through input–output grating couplers. Microring resonators were tuned with on-chip integrated titanium heating elements. The integrated heaters were used to alleviate any frequency mismatch of the coupled ring resonators, due to the coupling-induced resonance frequency shifting (CIFS) described in [14]. A number of >20 second- and third-order microresonator structures as well as >80 tapered or grating-coupled interfaces have been integrated on a 10.6 mm × 10.4 mm area of a 30 mm × 30 mm SOI chip revealing the high integration density of the approach. We demonstrate 40 Gb/s AOWC using the

second-order microstructures with power penalties <2.2 dB. In addition, we demonstrate 160 Gb/s AOWC assisted by the third-order microresonators with power penalties <3 dB. In the future, die-to-wafer bonding and heterogeneous III–V to SOI integration can be employed for large chip-scale integration of the resonator-assisted AOWCs [15].

II. MODELING

In this section, we describe the design of the microresonator structures. The modeling tools that have been employed are as follows: 1) ASPIC for generation of ring-resonator transfer functions using waveguide macroscopic parameters; 2) VPI for system-level AOWC evaluation; and c) a beam propagation tool for waveguide size and gap calculation. First, physical characteristics such as ring radius, attenuation of waveguides, group refractive index and power coupling coefficients between nanowires were inserted as parameters into ASPIC. For each parameter combination, ASPIC was generating a corresponding frequency and phase response which was loaded as input to a VPI-based WC modeling platform. The VPI setup comprised an SOA with 30 ps recovery time, a filtering module with the ASPIC transfer function, and a 2 ps passive delay interferometer (DI). The WC process is based on the chirp-filtering method [16]. Fig. 1(a) depicts the principle operation. A data stream and a local continuous wave (CW) are injected into the SOA for cross-gain modulation and cross-phase modulation (XGM-XPM). Due to the finite recovery time of the SOA, the WC signal is distorted. To accelerate signal performance, chirp filtering is employed using the response of a higher order ring resonator. With slight blue-shift offset filtering, an inverted WC signal is obtained while with larger filter detuning carrier suppression is achieved resulting in a non-inverted waveform. Signal polarity inversion for data rates >40 Gb/s is being performed with a DI using its spectral notch for carrier suppression. Far-offset filtering cannot be implemented since filter detuning is larger, losses increase and postamplification becomes not optimum.

The first simulations were performed at data rates up to 40 Gb/s. For effective chirp filtering, the drop-transmission ports of second-order microring components were utilized with 500 GHz free spectral range (FSR), 60 GHz 3 dB bandwidth, and 20 dB out of band suppression. Fig. 1(b) depicts the back-to-back data signal entering into the SOA encoded with a pseudorandom bit sequence (PRBS) $2^7 - 1$ and 2 ps pulsewidth. When the frequency response of the ring was centered on the peak of the WC signal, the recovery time of the SOA was evident as illustrated in Fig. 1(c). With 40 GHz blue shift, the recovery of the converted signal was accelerated leading to an open but inverted eye as shown in Fig. 1(d).

The cascaded DI with 2 ps differential delay could subsequently restore the polarity to a non-inverted format as depicted in Fig. 1(e). The resulting waveform had very low pedestal and very well shaped pulses. The carrier frequency of the original signal was 193.6 THz, while the CW signal powering the wavelength converting scheme was 193.1 THz.

For operation at 160 Gb/s, the second-order ring structure was not suitable due to the narrow 3 dB bandwidth and low out-band suppression filter profile. For this reason, a third-order
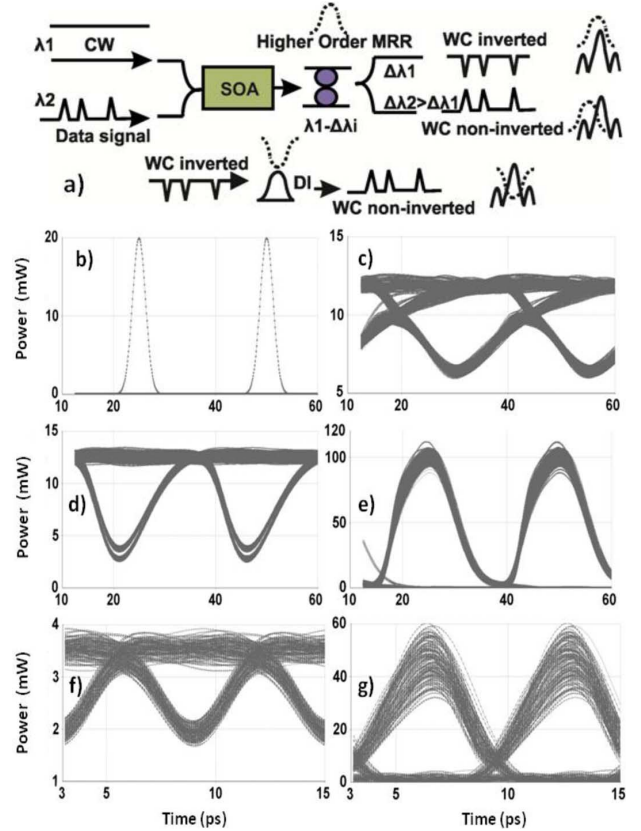

Fig. 1. (a) WC principle. (b) Back-to-back (B2B) signal. (c) Recovery of the SOA. (d) 40 Gb/s inverted WC. (e) 40 Gb/s non-inverted WC. (f) 160 Gb/s inverted WC. (g) 160 Gb/s non-inverted WC.

ring resonator was designed with 4 THz FSR, 190 GHz bandwidth, and 30 dB out of band suppression. By blue shifting the third-order ring resonator 120 GHz off the peak of the converted signal, the effective recovery time was accelerated as illustrated in Fig. 1(f). Pulse polarity was again restored with a DI obtaining a clear eye diagram with low pedestal as depicted in Fig. 1(g). The frequencies of the data stream and the CW injected into the AOWC were 194.6 and 193.1 THz, respectively.

Given the spectral characteristics of the second- and third-order microrings, the next step was to define the appropriate sizes and waveguide gaps. A beam propagation mode custom design tool was employed to extract the specifications listed in Table I for different microresonator structures. Racetrack resonators are believed to have more relaxing fabrication tolerances due to their longer interaction length resulting in a larger gap for a certain coupling.

III. DEVICE FABRICATION (FIRST RUN)

The fabrication of high-order silicon microring resonator filters requires high-resolution lithography. Electron beam lithography (EBL) has been employed for fabricating micro structures on SOI substrates with a top silicon layer of 220 nm on top of a 2 μm thick buried oxide. Hydrogen silsesquioxane (HSQ) has been used as negative tone resist to define waveguides, resonators, as well as auxiliary structures such as markers for the alignment of further exposures. A high contrast development process utilizing high concentrated tetra-methyl ammonium hydroxide as developer solution has been used [17]. The e-beam

TABLE I
SPECIFICATIONS FOR HIGHER ORDER MICRORESONATOR STRUCTURES

Structure / Parameter	2nd Order Ring	2nd Order Racetrack	3rd Order Ring	3rd Order Racetrack
FSR	4nm	4nm	27nm	12nm
Bending radius	23μm	15μm	3μm	5μm
Straight section length	-	25.5μm	-	8.5μm
Waveguide height	220nm	220nm	220nm	220nm
Waveguide width	450nm	450nm	500nm	450nm
Bus waveguide width	450nm	450nm	300nm	450nm
Gap bus-ring waveguide	85nm	290	90nm	160nm
Gap ring-ring waveguide	195nm	415nm	220nm	280nm

Fig. 2. (a) Cross-sectional SEM micrograph of etched test structure. (b) Semi-cross-sectional SEM micrograph of etched device structures.

Fig. 3. SEM micrograph of (a) third-order ring and (b) bus–ring coupling gap.

Fig. 4. (a) Waveguide taper tip structure. (b) SU-8-cladded waveguide.

dose has been selected to generate correct waveguide width in the HSQ resist. No proximity effect corrections were applied. A detailed analysis of the critical dimensions of the design such as coupling gaps, waveguide widths, or ring and racetrack widths has been carried out revealing that the resulting changes with respect to the designs critical dimensions were ±5 nm.

The structures have been transferred into the top silicon layer by means of inductively coupled plasma reactive ion etching (ICP-RIE). The etching process used is mainly based on HBr-chemistry. In a first step, pure HBr is used to achieve a highly anisotropic etch profile. The etching time for this first step is tuned so that a residual top silicon layer of about 10 nm remains on the substrate. The second step uses an admixture of O_2 to increase the selectivity between silicon and silica etching, resulting in a good etch stop on the buried oxide layer [18]. Fig. 2(a) demonstrates the high quality of the etching process showing a cross-sectional SEM micrograph of test structures etched with the same process. Fig. 2(b) shows a semicross-sectional view of an etched sidewall, visualizing the low-surface roughness of the structures. Fig. 3(a) depicts a third-order ring resonator with 3 μm bending radius, while Fig. 3(b) shows the 75 nm coupling gap obtained between the bus and ring waveguide. After structure transfer of the resist mask into the substrate material via ICP-RIE, the fabricated chips have again been inspected by SEM. The waveguide width, nominal cross section 450 nm × 220 nm, has been measured for different types of structures (straight waveguide, ring, and racetrack) and in different areas of the chip. A slight increase of the waveguide width measured after the etching compared to the width measured after EBL processing has been observed demonstrating both good critical dimension control and steepness of the resulting etch profile.

To enable efficient fiber-to-chip coupling, SU8 spot size converters have been integrated into the design [19]. Therefore, the silicon waveguide ends have been designed with narrow tips of about ∼40 nm width. In Fig. 4(a), an etched waveguide taper tip is shown in an SEM micrograph. In a second EBL step, those tapered waveguide ends have been covered with a fiber size SU-8 cladding waveguide which allows high-efficiency coupling, as
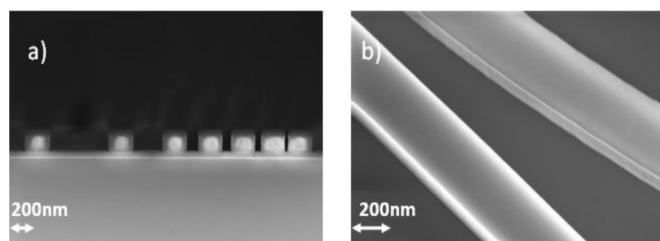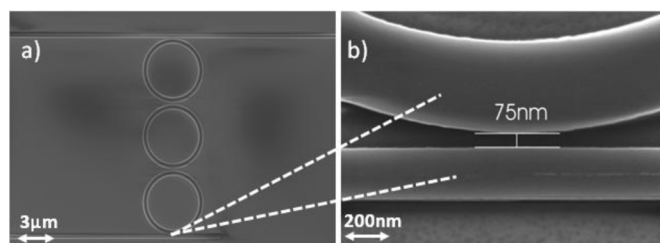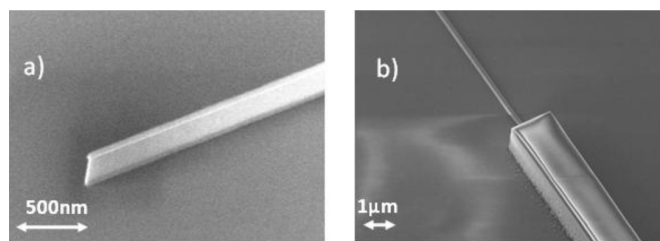
depicted in Fig. 4(b). The whole fabrication process, consisting of pattern processing, electron beam exposure, development, pattern transfer, and definition of the cladding waveguide, has been optimized with respect to different quality parameters such as side wall roughness, critical dimension control, and high coupling efficiencies to guarantee a good performance of the devices fabricated.

IV. DEVICE FABRICATION (SECOND RUN)

In the next fabrication run, heating elements have been incorporated in the microcomponents for 1) compensating any fabrication tolerances that would lead to gap variations and frequency mismatch; and 2) making the wavelength-selective switches fully functional and reconfigurable. The integration of heating elements on top of the SOI photonic layer required, however, a cladding that would serve as a spacer. The spacer was essential since the metal should not lie directly on top of the SOI photonic layer. The reason is that due to the evanescent field, the light is absorbed by the metal, and thus decreasing the performance of the ring. Fig. 5(a) shows a cross section of the layer structure: the SOI waveguide (ring) with a cross section of 450 nm × 220 nm is placed on top of the buried oxide (BOX). An additional SiO_2 layer with 800 nm thickness is deposited by spin coating. The metal that is used for the heating elements is titanium with a thickness of 100 nm. The heating elements are structured by a lift-off process, and they are designed for
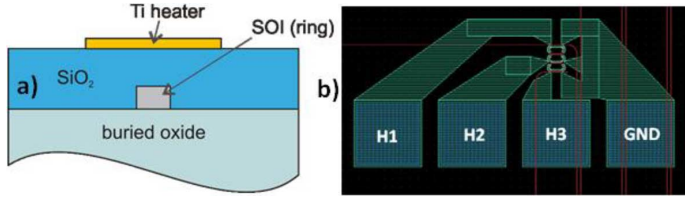
Fig. 5. (a) Cross section of an SOI waveguide (ring) with SiO_2 cladding and Ti as heating metal on top. (b) Layout of heating elements on top of a third-order SOI ring resonator.
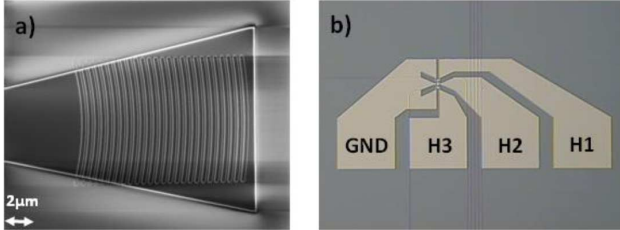

Fig. 6. (a) SEM picture of fabricated grating coupler. (b) Optical microscope image of a third-order ring resonator with heating elements.
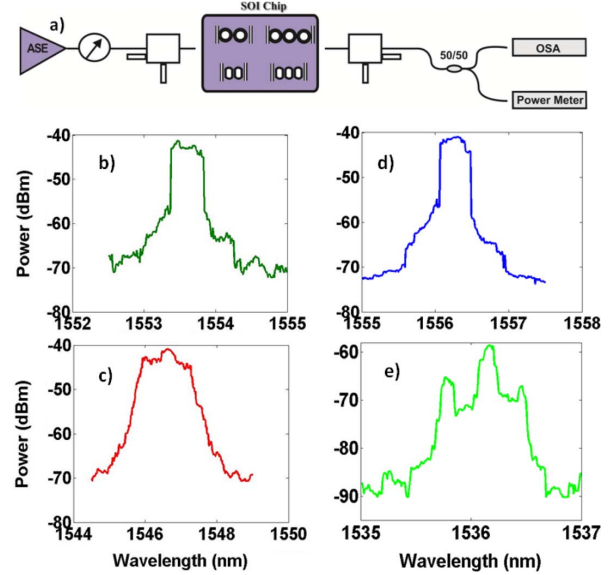

Fig. 7. (a) Optical characterization setup. Drop transmission responses of (b) second-order racetrack, (c) third-order racetrack, (d) second-order ring, and (e) third-order ring.

effective temperature variation along the ring elements without affecting the coupling regions in a deteriorating way. Their layout for a third-order ring resonator is depicted in Fig. 5(b). All the integrated heaters can be enabled using four metal pads: one common ground and 3 pads for driving the heater of each coupled ring resonator.

The fabrication procedure has been started with the definitions of waveguide and resonator devices by EBL. To integrate the shallow etched grating couplers, a process flow which allows the combination of fully etched strip waveguides with partially etched grating couplers has been developed. For that purpose, the silicon waveguide ends have been designed as wide triangular area. This area is shown in Fig. 6(a) and is defined in a first EBL step together with the waveguides and resonators. The defined pattern has been transferred into the top silicon layer by means of ICP-RIE. The top silicon layer has been fully etched down to the buried oxide. Then, the grating is realized in the triangular area at the waveguide ends employing additional EBL and ICP-RIE steps. For the definition of the gratings on the prestructured samples, the positive tone electron sensitive resist ZEP 520A has been used. The EBL is followed by shallow etching. An overview of a fabricated grating coupler is shown in Fig. 6(a). As the overlap of the grating into the buried oxide region is almost equal for both the top and the bottom edge of the coupler, the overlay accuracy between the two different EBL steps is very good. In the next fabrication steps, the heater elements were integrated on top of the higher order resonator structures. A spin-on-glass (SOG) cladding has been chosen for the separation of the waveguide from the heater. The SOG material has been deposited by spin coating. On top of the SOG material the heater elements, depicted in Fig. 6(b), have again been defined by EBL using poly(methyl methacrylate) resist. After pattern definition, a 100 nm thick titanium layer has been deposited by electron beam evaporation and the heating elements have been structured by a lift-off process.

V. OPTICAL CHARACTERIZATION

Fig. 7(a) depicts the experimental setup for the characterization of the SOI components. Amplified spontaneous emission from a *C*- and *L*-band erbium-doped fiber amplifier was combined for capturing the microresonator responses. A single polarization state was preserved utilizing a polarizer with over 30 dB polarization extinction ratio. The light was coupled into the chip through polarization maintaining lensed fibers and the spectral responses were acquired by an optical spectrum analyzer with a resolution of 10 pm.

Fig. 7 illustrates the drop filter responses from the first generation microstructures with SU8 cladding. Fig. 7(b) and (d) depicts the spectral profiles of the second-order microstructures with sharp and box-shaped profile and out-band suppression around 14 dB. Fig. 7(c) and (e) depicts the filtering characteristics of third-order resonators. The third-order racetracks exhibit a well-shaped resonance with optimum spectral overlap between the individual coupled racetracks and a higher out-band suppression with respect to second-order elements. The third-order microring resonators on the other hand reveal a frequency mismatch—with degenerated peaks-clearly visible in Fig. 7(e). This frequency mismatch can be attributed to the CIFS, counteracted by design [14], and to lithographic imperfections. The lower insertion loss measured in racetrack resonators compared to that in ring resonators was attributed to the longer coupling regions between the bus–racetrack and racetrack–racetrack waveguides, the larger spacing between the bus–racetrack and racetrack–racetrack waveguides as well as to the their more relaxing fabrication tolerances. Table II outlines some additional values collected during optical characterization. The FSR measured was near the design specifications of Table I, while the 3 dB bandwidth and out-band suppression was sufficient for 40 and 160 Gb/s system tests. The fiber-to-fiber losses have been calculated as low as ~11 dB verifying the 50% SU8 coupling efficiency.

TABLE II
CHARACTERIZATION RESULTS FOR FIRST/SECOND RUN MICROSTRUCTURES

Structure Parameter	2nd Order Ring	2nd Order Racetrack	3rd Order Ring	3rd Order Racetrack
FSR	3.6/3.8nm	3.6/3.8nm	26/28nm	11/12nm
3dB BW	0.4/0.6nm	0.5/0.7nm	0.3/1.4nm	1.4/1.4nm
Out-band suppression	13/15dB	14/16dB	17/22dB	25/26dB
Fiber-to-Fiber losses	12/29dB	11/28dB	29/40dB	12/29dB

The high loss obtained for the third-order ring resonator was attributed to the ring resonator spectral mismatch.

This frequency mismatch observed was corrected with the integration of Ti heaters on top of the ring structures. For their fabrication and metal deposition, an additional SiO_2 layer was required precluding the use of SU8 tapers for input–output coupling. As an alternative, grating couplers were fabricated with 30% efficiency and spectral profile depicted in Fig. 8(a). It is clearly shown that the response was optimized for wavelengths centred to 1580 nm. Fig. 8(b) illustrates the wavelength tuning characterization results for the third-order ring resonator. Without applying voltage in the integrated heating element, three major peaks were evident due to the spectral mismatch of the ring structures. When increasing the current at the heater H1 [see Fig. 5(b)], the left resonance peak of the underlying SOI ring was red shifted 2 nm and the center peak 1 nm resulting to frequency overlapping with the third ring resonance. The reason for the spectral shift of two resonances with a single heater is attributed to the lack of thermal isolation between the coupled ring resonators as well as to their very close proximity (<90 nm). Assuming a maximum power of approximately 7.25 mW a tuning range of 5.6 nm was obtained. Table II outlines also the optical characterization results for the second-run devices. Similar spectral characteristics have been observed but with rather higher losses due to the utilization of grating couplers. The typical fiber-to-fiber loss for a reference waveguide was ∼17 dB. The higher 3 dB bandwidth and the out-band suppression value for the third-order ring resonator was attributed to properly tuned and coupled resonances using the integrated heating elements.

VI. EXPERIMENT

A. 40 Gb/s System Tests Using Second-Order SOI Resonators

Fig. 9 shows the experimental setup used for the system evaluation of the microresonators. The 40 Gb/s data signal was generated by a 2.2 ps, 40 GHz, tunable, mode-locked laser modulated with a $2^7 - 1$ PRBS. A pigtailed commercially available SOA with a gain recovery time of 30 ps was used for XGM-XPM. A tunable laser provided the CW signals. Fiber-to-chip coupling was performed through standard single-mode lensed fibers. The data signal was injected into the SOA together with the CW light using an optical combiner. Due to the finite recovery time of the SOA, the WC signal was distorted causing intersymbol interference (ISI). By detuning the CW to a larger
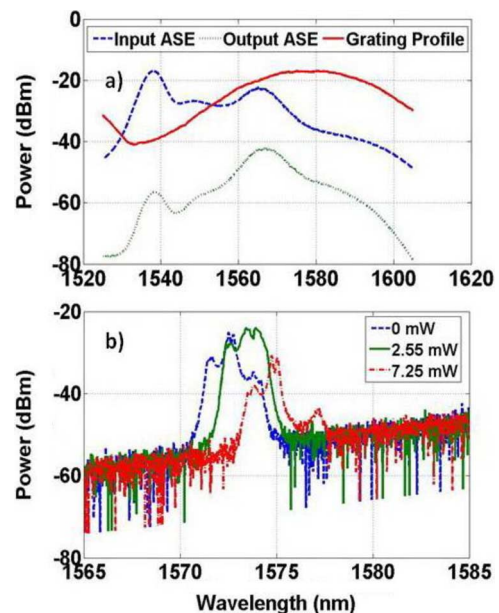

Fig. 8. (a) Grating coupler filter response. (b) Wavelength tuning of third-order ring resonator when heater H1 is enabled.

wavelength away from the microresonator drop resonance, the effective recovery time was accelerated suppressing ISI. The WC signal, however, was in inverted mode since the CW carrier was dominant with respect to the data harmonic. Signal polarity restore was implemented by further CW detuning so as the falling edge of the microresonance to coincide with the CW carrier. This had, as a consequence, the carrier component to be suppressed and the data harmonic to become dominant [20]. After polarity inversion the WC signal was evaluated with bit-error-rate (BER) measurements after performing demultiplexing to 10 Gb/s using an electroabsorption modulator.

Fig. 10(a) illustrates the eye diagram of the 40 Gb/s back-to-back data signal. By detuning the CW 0.7 nm off the second-order racetrack filter response, the WC signal of Fig. 10(b) was recorded. The waveform had additional noise since inversion was implemented with far filtering resulting to low output power and not optimum amplification. Fig. 10(c) shows the eye diagram obtained using the second-order microring resonator. The performance deterioration is due to the higher insertion loss and smaller out-band suppression (see Table II) of the ring resonator. The broadening of the pulses for both resonant configurations was attributed to the relative narrow 3 dB bandwidth ∼0.4 nm. Fig. 10(d) depicts the BER curves. Error-free operation was achieved for all the channels with 1.1 and 2.2 dB power penalty for the racetrack and ring resonator respectively. Fig. 10(e) shows the spectra of the 40 Gb/s WC and data signal after the SOA. In order to perform chirp filtering as well as polarity inversion, the response of a second-order racetrack was employed, blue shifted with respect to the WC carrier. Since the falling edge of the second-order racetrack had a sharp spectral profile, the blue-shift filtering had, as a consequence, the WC carrier suppression and the polarity inversion of the WC signal in time domain. Fig. 10(f) depicts the 40 GHz harmonic that has become dominant and the WC carrier that has been effectively suppressed. Fig. 10(g) and (h) illustrates the WC spectra using a
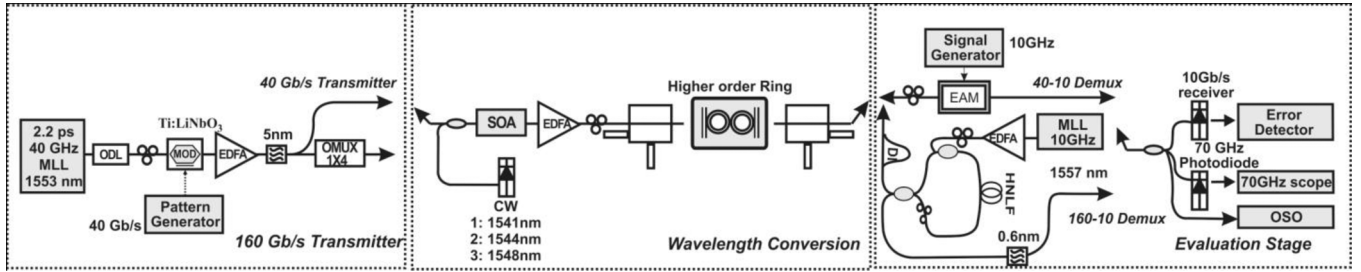
Fig. 9. Experimental setup for evaluation of the second- and third-order microresonator components.
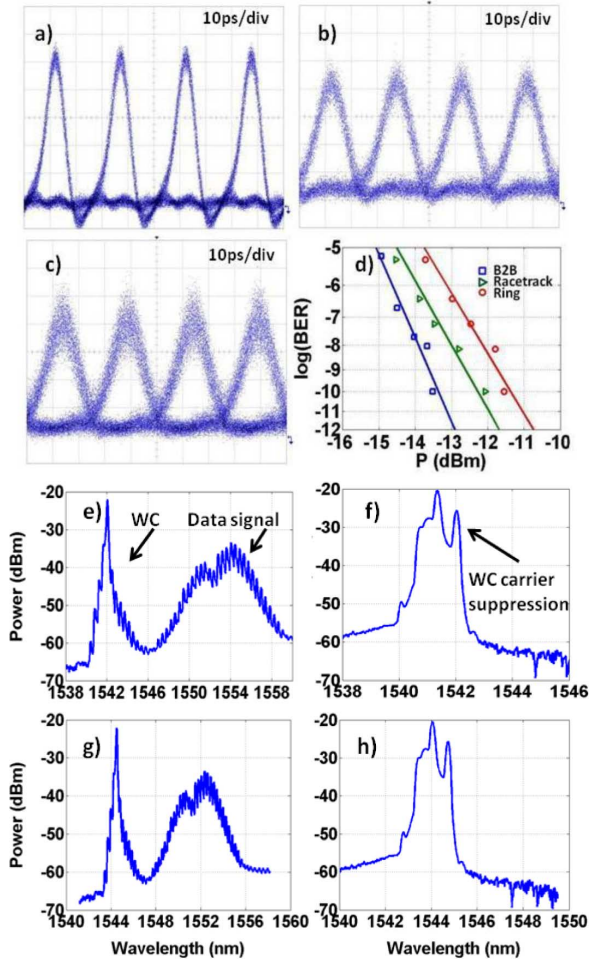

Fig. 10. (a) 40 Gb/s B2B. (b) WC with the second-order racetrack. (c) WC signal with the second-order ring. (d) BER curves. Spectra (e), (f) after SOA and second-order racetrack, (g), (h) after SOA and second-order ring, respectively.
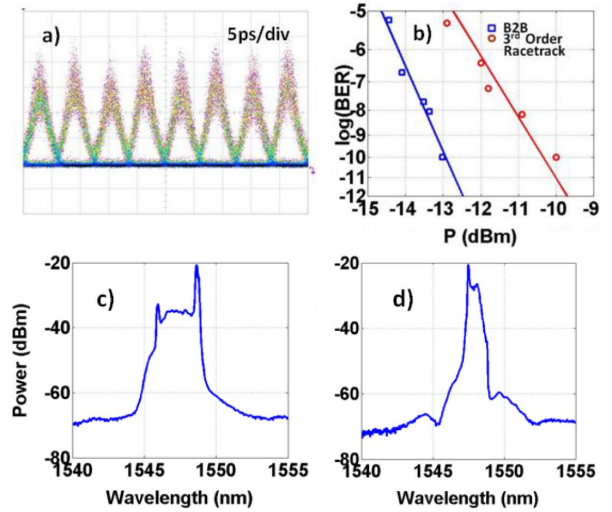

Fig. 11. (a) 160 Gb/s WC signal using a third-order racetrack. (b) BER curves for B2B and WC signal. Spectra: (c) inverted WC signal and (d) non-inverted signal after the DI.

second-order ring resonator. Initial and converted wavelengths for both cases were 1) 1553 to 1541 nm; and 2) 1553 to 1544 nm.

B. 160 Gb/s System Tests Using Third-Order Devices

Fig. 9 illustrates the experimental setup used for the 160 Gb/s system measurements. The 160 Gb/s data signal was generated by time multiplexing the 40 Gb/s transmitter through a fiber interleaver. Using this stream together with a local CW, WC was performed in the SOA. The slow recovery time was accelerated by employing the filter response of the third-order racetrack

as chirp-filtering element. Signal polarity was subsequently restored utilizing a 2 ps DI. At the receiver side the WC signal was evaluated after performing 160 to 10 Gb/s optical demultiplexing using a nonlinear loop mirror (NOLM). The nonlinear element of the NOLM was 100 m of HNLF with 10 W^{-1}km^{-1} nonlinear parameter and 1.21 ps/nm/km dispersion. As control signal into the NOLM, a mode-locked laser at 1557 nm was utilized emitting 1.3 ps optical pulses at 10 GHz repetition rate. Fig. 11(a) shows the non-inverted WC signal recorded with an optical sampling oscilloscope (OSO). From the OSO trace, it is evident that the out-band suppression and bandwidth of the third-order racetrack was sufficient for speeding up the SOA and enable 160 Gb/s operation. Fig. 11(b) depicts the BER curves obtained after optical demultiplexing. The power penalty was measured ~3 dB, which is close to the power penalty obtained using bulk, and customized optical bandpass filters for chirp filtering [16]. Fig. 11(c) and (d) illustrates the spectra of the 160 Gb/s WC signal in the inverted and non-inverted mode respectively. In fact, Fig. 11(c) presents the spectrum after the third-order racetrack when 1.2 nm blue-shift offset filtering has been performed. In order to restore the polarity of the WC signal in time domain, a DI was applied whose spectral notch was centered to the WC carrier. Fig. 11(d) depicts the effective carrier suppression by the DI. Signal polarity inversion using only the spectral response of the third-order racetrack was not feasible since the required offset filtering was too large resulting

to high losses and not-optimum amplification. The third-order ring structures could not be experimentally tested due to the high fiber-to-fiber losses ($\sim$39 dB). Our current study is focused on the grating coupler design and fabrication optimization [21] in order to minimize loss and allow subsequent system testing.

VII. CONCLUSION

We have demonstrated the design, fabrication, and experimental evaluation of nanophotonic structures for microresonator-assisted all-optical wavelength converters. First, we have specified all the physical parameters using appropriate modeling tools. We reported two fabrication runs based on high-resolution e-beam lithography for the development of the second- and third-order microring and racetrack resonators. We demonstrate error-free WC up to 160 Gb/s employing the nanowire periodic filters. Power penalties $<$3 dB have been obtained making the use of microresonators promising for scalable and power-efficient AOWC.

ACKNOWLEDGMENT

REFERENCES

[1] B. Jalali and S. Fathpour, "Silicon photonics," *J. Lightw. Technol.*, vol. 24, no. 12, pp. 4600–4615, Dec. 2006.

[2] N. Izhaky, M. T. Morse, S. Koehl, O. Cohen, D. Rubin, A. Barkai, G. Sarid, R. Cohen, and M. J. Paniccia, "Development of CMOS-compatible integrated silicon photonics devices," *IEEE J. Sel. Topics Quantum Electron.*, vol. 12, no. 6, pp. 1688–1698, Nov./Dec. 2006.

[3] S. Janz, P. Cheben, D. Dalacu, A. Delage, A. Densmore, B. Lamontagne, M. J. Picard, E. Post, J. H. Schmid, P. Waldron, D. X. Xu, K. P. Yap, and W. N. Ye, "Microphotonics elements for integration on the silicon-on-insulator waveguide platform," *IEEE J. Sel. Topics Quantum Electron.*, vol. 12, no. 6, pp. 1402–1415, Nov./Dec. 2006.

[4] T. Tsuchizawa, K. Yamada, H. Fukuda, T. Watanabe, J. Takahashi, M. Takashi, T. Shoji, E. Tamechica, S. Itabashi, and H. Morita, "Microphotonics devices based on silicon microfabrication technology," *IEEE J. Sel. Topics Quantum Electron.*, vol. 11, no. 1, pp. 232–240, Jan./Feb. 2005.

[5] W. Bogaerts, P. Dumon, D. Van Thourhout, D. Taillaert, P. Jaenen, J. Wouters, S. Beckx, V. Wiaux, and R. G. Baets, "Compact wavelength-selective functions in silicon-on-insulator photonic wires," *IEEE J. Sel. Topics Quantum Electron.*, vol. 12, no. 6, pp. 1394–1401, Nov./Dec. 2006.

[6] U. Plachetka, N. Koo, T. Wahlbrink, J. Bolten, M. Waldow, T. Plötzing, M. Först, and H. Kurz, "Fabrication of photonic ring resonator device in silicon waveguide technology using soft UV-nanoimprint lithography," *IEEE Photon. Technol. Lett.*, vol. 20, no. 7, pp. 490–492, Apr. 2008.

[7] S. T. Chu, B. E. Little, V. Van, J. V. Hryniewicz, P. P. Absil, F. G. Johnson, D. Gill, O. King, F. Seiferth, M. Trakalo, and J. Shanton, "Compact full C-band tunable filters for 50 GHz channel spacing based on high-order micro-ring resonators," presented at the presented at the Opt. Fiber Commun. Conf., Los Angeles, CA, 2004, Paper PDP9.

[8] B. G. Lee, A. Biberman, N. Sherwood-Droz, C. B. Poitras, M. Lipson, and K. Bergman, "High-speed 2 × 2 switch for multiwavelength silicon- photonic networks-on-chip," *J. Lightw. Technol.*, vol. 27, no. 4, pp. 2900–2907, Jul. 2009.

[9] F. Xia, L. Sekaric, and Y. Vlasov, "Ultra-compact optical buffers on a silicon chip," *Nature Photon.*, vol. 1, pp. 65–71, 2007.

[10] N. Ophir, K. Padmaraju, A. Biberman, L. Chen, K. Preston, M. Lipson, and K. Bergman, "First demonstration of error-free operation of a full silicon on-chip photonic link," presented at the presented at the Opt. Fiber Commun. Conf., Los Angeles, CA, 2011, Paper OWZ3.

[11] K. Vyrsokinos, L. Stampoulidis, Z. Sheng, E. Kehayas, P. Bakopoulos, D. Petrantonakis, C. Stamatiadis, Ch. Kouloumentas, P. Zakynthinos, R. Dekker, E. J. Klein, D. Van Thourhout, M. T. Kothorst, and H. Avramopoulos, "Higher-order micro-ring resonator assisted wavelength converters for scalable and power efficient photonic routers," presented at the presented at the Eur. Conf. Opt. Commun., Vienna, Austria, 2009, Paper P2.08.

[12] C. Stamatiadis, D. Petrantonakis, P. Bakopoulos, E. Kehayas, P. Zakynthinos, Ch. Kouloumentas, L. Stampoulidis, Z. Sheng, E. Kehayas, P. Bakopoulos, D. Petrantonakis, C. Stamatiadis, C. Kouloumentas, P. Zakynthinos, R. Dekker, E. J. Klein, D. Van Thourhout, M. T. Kothorst, and H. Avramopoulos, "First demonstration of WDM-enabled all-optical wavelength conversion with a SOA and a 2nd order micro-ring resonator ROADM," presented at the presented at the Opt. Fiber Commun. Conf., San Diego, CA, 2009, Paper PDPA8.

[13] C. Stamatiadis, K. Vyrsokinos, L. Stampoulidis, A. Maziotis, Z. Sheng, D. Van Thourhout, J. Bolten, M. Karl, T. Wahlbrink, and H. Avramopoulos, "All-optical wavelength conversion at 160 Gb/s using an SOA and a 3rd order SOI nanowire periodic filter," presented at the presented at the IEEE Photon. Soc. Annu. Meet. 2010, Denver, CO, 2010.

[14] M. Popovic, M. Watts, T. Barwicz, P. Rakich, L. Socci, E. Ippen, F. Kartner, and H. Smith, "High-index-contrast, wide-FSR microring-resonator filter design and realization with frequency-shift compensation," presented at the presented at the Opt. Fiber Commun. Conf., Anaheim, CA, 2005, Paper OFK1.

[15] L. Liu, T. Spuesens, D. Van Thourhout, G. Morthier, L. Grenouillet, N. Olivier, J. Fedeli, P. Romeo, P. Régreny, F. Mandorlo, and R. Orobtchouk, "200 mm wafer scale III-V/SOI technology for all-optical network-on-chip and signal processing," presented at the presented at the 7th IEEE Int. Conf. Group IV Photon. (GFP), Beijing, China, 2010.

[16] Y. Liu, E. Tangdiongga, Z. Li, H. de Waardt, A. M. J. Koonen, G. D. Khoe, and H. J. S. Dorren, "Error-free 320 Gbit/s SOA-based wavelength conversion using optical filtering," presented at the presented at the Opt. Fiber Commun. Conf., Anaheim, CA, 2006, Paper PDP28.

[17] W. Henschel, Y. M. Georgiev, and H. Kurz, "Study of a high contrast process for hydrogen silsesquioxane as a negative tone electron beam resist," *J. Vac. Sci. Technol. B21*, vol. 5, pp. 2018–2024, 2003.

[18] T. Wahlbrink, T. Mollenhauer, Y. M. Georgiev, W. Henschel, J. K. Efavi, H. D. B. Gottlob, M. C. Lemme, H. Kurz, J. Niehusmann, and P. H. Bolivar, "Highly selective etch process for silicon-on-insulator nano devices," *Microelectron. Eng.*, vol. 78–79, pp. 212–217, 2005.

[19] T. Wahlbrink, W. S. Tsai, M. Waldow, M. Först, J. Bolten, T. Mollenhauer, and H. Kurz, "Fabrication of high efficiency SOI taper structures," *Microelectron. Eng.*, vol. 86, pp. 1117–1119, 2009.

[20] J. Dong, X. Zhang, S. Fu, J. Xu, P. Shum, and D. Huang, "Ultrafast all-optical signal processing based on single semiconductor optical amplifier and optical filtering," *IEEE J. Sel. Topics Quantum Electron.*, vol. 14, no. 3, pp. 770–778, May/Jun. 2008.

[21] D. Vermeulen, S. Selvaraja, P. Verheyen, G. Lepage, W. Bogaerts, P. Absil, D. Van Thourhout, and G. Roelkens, "High-efficiency fiber-to-chip grating couplers realized using an advanced CMOS-compatible silicon-on-insulator platform," *Opt. Exp.*, vol. 18, pp. 18278–18283, 2010.

Author biographies not included at author request due to space constraints.